# 星形成ゼミ
2018/02/16
SFN #300 #51-#60

長谷川哲夫（国立天文台）

## 300 Dust Concentration and Emission in Protoplanetary Disks Vortices

#51 Anibal Sierra1, Susana Lizano1 and Pierre Barge2
ApJ 850,115 (2017)

We study the dust concentration and emission in protoplanetary disks vortices. We extend the Lyra-Lin solution for the dust concentration of a single grain size to a power-law distribution of grain sizes $n(a) \propto a^{-p}$. Assuming dust conservation in the disk, we find an analytic dust surface density as a function of the grain radius. We calculate the increase of the dust to gas mass ratio ϵ and the slope p of the dust size distribution due to grain segregation within the vortex. We apply this model to a numerical simulation of a disk containing a persistent vortex. Due to the accumulation of large grains towards the vortex center, ϵ increases by a factor of 10 from the background disk value, and p decreases from 3.5 to 3.0. We find the disk emission at millimeter wavelengths corresponding to synthetic observations with ALMA and VLA. The simulated maps at 7 mm and 1 cm show a strong azimuthal asymmetry. This happens because, at these wavelengths, the disk becomes optically thin while the vortex remains optically thick. The large vortex opacity is mainly due to an increase in the dust to gas mass ratio. In addition, the change in the slope of the dust size distribution increases the opacity by a factor of 2. We also show that the inclusion of the dust scattering opacity substantially changes the disks images.
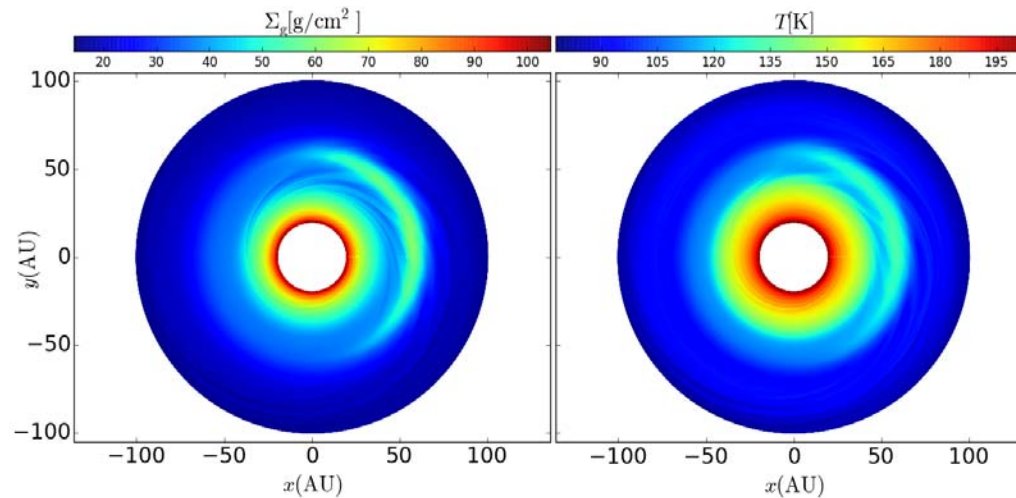
Figure 1. Gas surface density (left) and gas temperature (right) of a disk containing a large scale vortex (after 100 vortex rotations) .
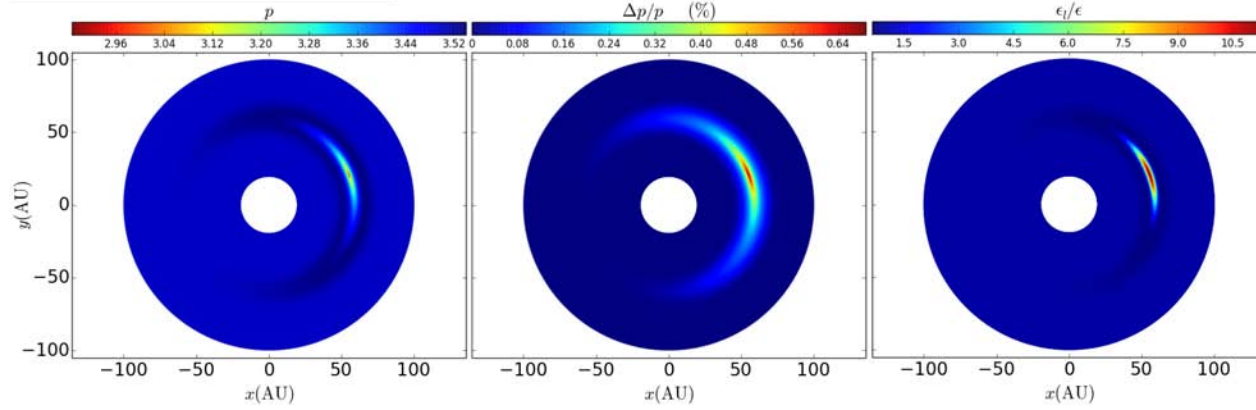
Figure 2. Dust particle accumulation within the vortex. Left panel: Slope p of the power law fit to the dust particle size distribution $n(a)da \propto a^{-p}da$ (see text). Middle panel: fractional standard deviation $\Delta p/p$. Right panel: Map of the local dust to gas mass ratio (normalized
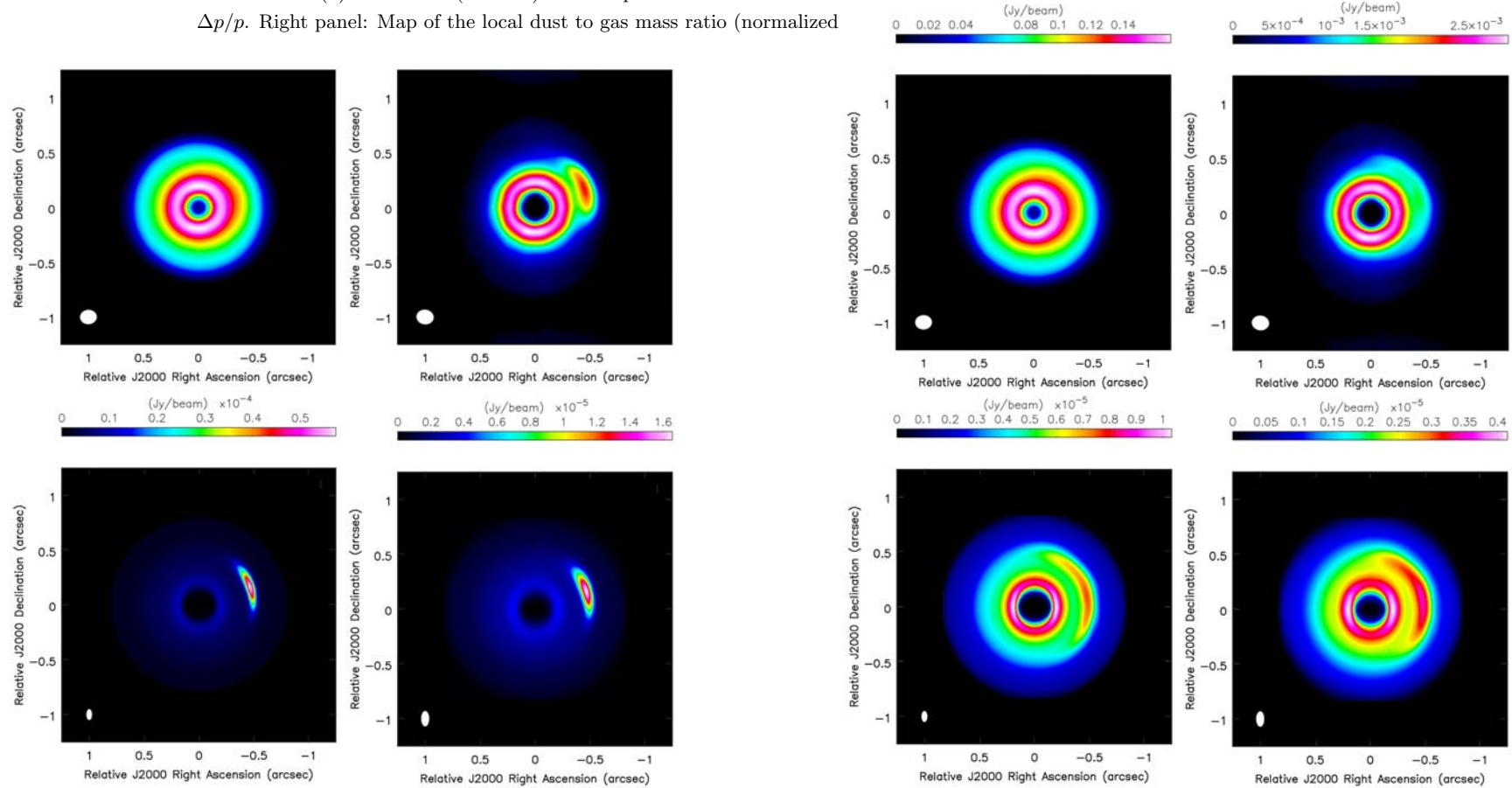

Figure 3. Upper panels: Simulated ALMA images at 1 mm (left) and 3 mm (right). Lower panels: Simulated VLA images at 7 mm (left) and 1 cm (right). The beam is shown in the left bottom corner of each image.

Figure 5. Upper panels: Simulated ALMA images at 1 mm (left) and 3 mm (right). Lower panels: Simulated VLA images at 7 mm (left) and 1 cm (right). These models do not include dust segregation inside the vortex (see text). The beam is shown in the left bottom corner of each image.

300 ALMA Reveals Transition of Polarization Pattern with Wavelength in HL Tau's Disk

#52   Ian W. Stephens1, Haifeng Yang2, Zhi-Yun Li2, Leslie W. Looney3, Akimasa Kataoka4,5, Woojin Kwon6,7, Manuel Fern'andez-Lo'pez8, Charles L. H. Hull5,9,10, Meredith Hughes11, Dominique Segura- Cox3,12, Lee Mundy13, Richard Crutcher3 and Ramprasad Rao14

The mechanism for producing polarized emission from protostellar disks at (sub)millimeter wave- lengths is currently uncertain. Classically, polarization is expected from non-spherical grains aligned with the magnetic field. Recently, two alternatives have been suggested. One polarization mechanism is caused by self-scattering from dust grains of sizes comparable to the wavelength while the other mechanism is due to grains aligned with their short axes along the direction of radiation anisotropy. The latter has recently been shown as a likely mechanism for causing the dust polarization detected in HL Tau at 3.1 mm. In this paper, we present ALMA polarization observations of HL Tau for two more wavelengths: 870 μm and 1.3 mm. The morphology at 870 μm matches the expectation for self-scattering, while that at 1.3 mm shows a mix between self-scattering and grains aligned with the radiation anisotropy. The observations cast doubt on the ability of (sub)millimeter continuum polarization to probe disk magnetic fields for at least HL Tau. By showing two distinct polarization morphologies at 870 μm and 3.1 mm and a transition between the two at 1.3 mm, this paper pro- vides definitive evidence that the dominant (sub)millimeter polarization mechanism transitions with wavelength. In addition, if the polarization at 870 μm is due to scattering, the lack of polarization asymmetry along the minor axis of the inclined disk implies that the large grains responsible for the scattering have already settled into a geometrically thin layer, and the presence of asymmetry along the major axis indicates that the HL Tau disk is not completely axisymmetric.
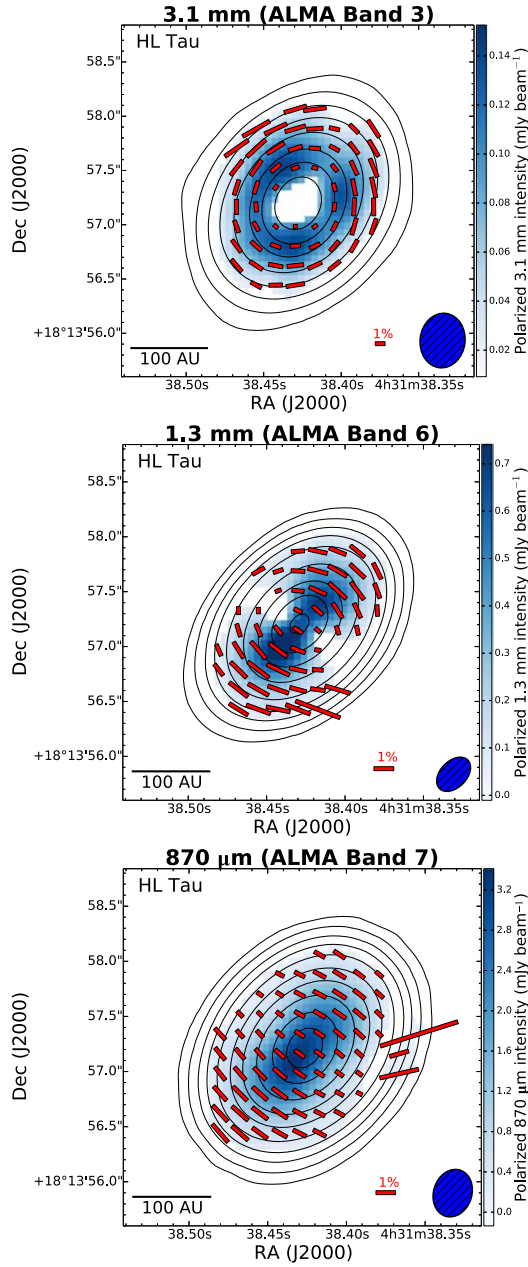
Figure 1. ALMA polarimetric observations at 3.1 mm (top, Kataoka et al. 2017), 1.3 mm (middle), and 870 μm (bottom), where the red vectors show the >3σ polarization morphology (i.e., vectors have not been rotated). Vector lengths are linearly proportional to *P*. The color scale shows the polarized intensity, which is masked to only show 3σ detections. Stokes *I* contours in each panel are shown for [3, 10, 25, 50, 100, 200, 325, 500, 750, 1000] × σ$_I$, where σ$_I$ is 44, 154, and 460 μJy bm^{-1} for 3.1 mm, 1.3 mm, and 870 μm, respectively.
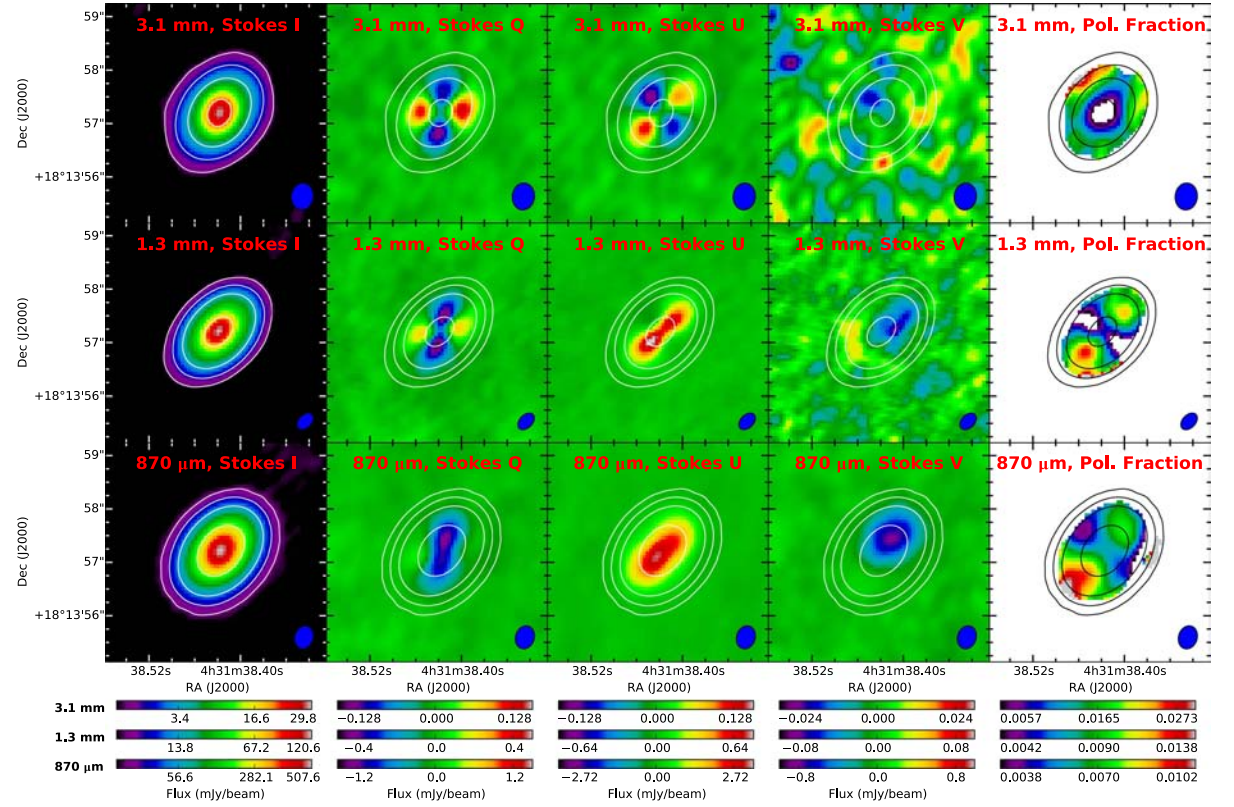
Figure 2. ALMA observations of the Stokes parameters *IQUV* and the linear polarization fraction *P* for 3.1 mm (top), 1.3 mm (middle), and 870 μm (bottom). Stokes *I* contours for a particular wavelength is shown in each panel for [4, 25, 100, 500] × σ$_I$, where σ$_I$ is given in Figure 1.
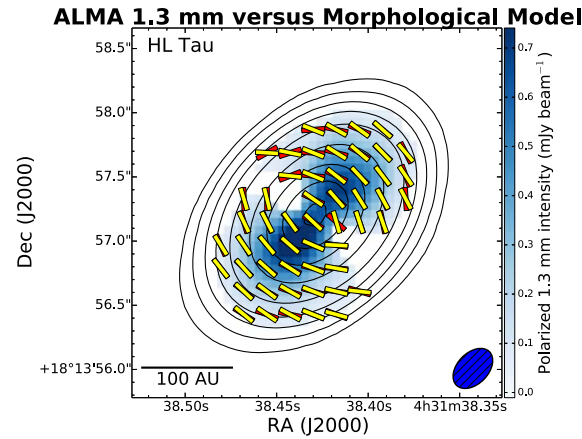
Figure 3. Morphological 1.3 mm model for a 50–50 mix of azimuthal and uniform patterns is shown with yellow vectors, which are overlaid on top of the observed polarization morphology (red vectors). The contours are Stokes *I*, with the levels given in Figure 1.
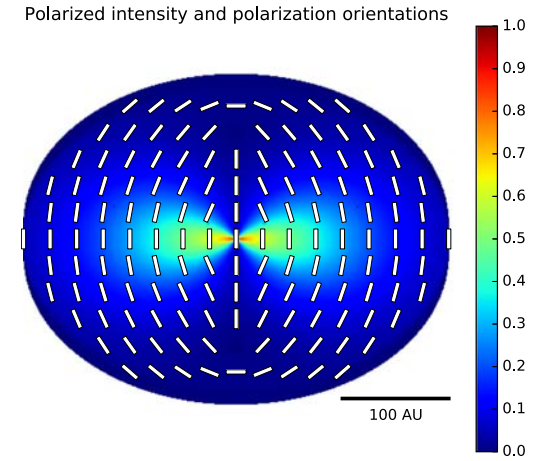
Figure 4. Distribution of polarized intensity with polarization vectors superposed for an illustrative disk model where the polarization is produced by a combination of direct emission and scattering by azimuthally aligned grains. Color scale has been normalized to have a peak of 1.

300 #53 The spatial extent of Polycyclic Aromatic Hydrocarbons emission in the Herbig star HD 179218

Anas S. Taha1, Lucas Labadie1, Eric Pantin2, Alexis Matter3, Carlos Alvarez4, Pilar Esquej5, Rebekka Grellmann1, Rafael Rebolo6, Charles Telesco7 and Sebastian Wolf8

A&A

We investigate, in the mid-infrared, the spatial properties of the Polycyclic Aromatic Hydrocarbons (PAHs) emission in the disk of HD 179218, an intermediate-mass Herbig star at $\sim$300 pc. We obtained mid-infrared images in the PAH-1, PAH-2 and Si-6 filters centered at 8.6, 11.3, and 12.5 μm, and N-band low-resolution spectra using CanariCam on the 10-m Gran Telescopio Canarias (GTC). We compared the point spread function (PSF) profiles measured in the PAH filters to the profile derived in the Si-6 filter, where the thermal continuum emission dominates. We performed radiative transfer modeling of the spectral energy distribution (SED) and produced synthetic images in the three filters to investigate different spatial scenarios. Our data show that the disk emission is spatially resolved in the PAH-1 and PAH-2 filters, while unresolved in the Si-6 filter. Thanks to very good observing conditions, an average full width at half maximum (FHWM) of 0.232″, 0.280″ and 0.293″ is measured in the three filters, respectively. Gaussian disk fitting and quadratic subtraction of the science and calibrator PSFs suggests a lower-limit characteristic angular diameter of the emission of $\sim$100 mas, or $\sim$30 au. The photometric and spectroscopic results are compatible with previous findings. Our radiative transfer (RT) modeling of the continuum suggests that the resolved emission should result from PAH molecules on the disk atmosphere being UV-excited by the central star. Simple geometrical models of the PAH component compared to the underlying continuum point to a PAH emission uniformly extended out to the physical limits of the disk model. Furthermore, our RT best model of the continuum requires a negative exponent of the surface density power-law, in contrast with earlier modeling pointing to a positive exponent. We have spatially resolved - for the first time to our knowledge - the PAHs emission in the disk of HD 179218 and set constraints on its spatial extent. Based on spatial and spectroscopic considerations as well as on qualitative comparison with IRS 48 and HD 97048, we favor a scenario in which PAHs extend out to large radii across the flared disk surface and are at the same time predominantly in an ionized charge state due to the strong UV radiation field of the $180\,L_{\odot}$ central star.

ATLASGAL-selected massive clumps in the inner Galaxy: VI. Kinetic temperature and spatial density measured with formaldehyde

X. D. Tang1,2,3, C. Henkel1,4, F. Wyrowski1, A. Giannetti1,5, K. M. Menten1, T. Csengeri1, S. Leurini1,6, J. S. Urquhart1,7, C. Koenig1, R. Guesten1, Y. X. Lin1, X. W. Zheng8, J. Esimbek2,3 and J. J. Zhou2,3
A&A

Formaldehyde (H_2CO) is a reliable tracer to accurately measure the physical parameters of dense gas in star forming regions. We aim to directly determine the kinetic temperature and spatial density with formaldehyde for the $\sim$100 brightest ATLASGAL-selected clumps (the TOP100 sample) at $870\,\mu$m representing various evolutionary stages of high-mass star formation. Ten transitions ($J=3$–2 and 4–3) of ortho- and para-H_2CO near 211, 218, 225, and 291 GHz were observed with the Atacama Pathfinder EXperiment (APEX) 12 m telescope. Using non-LTE models with RADEX, we derive the gas kinetic temperature and spatial density using the measured para-H_2CO 3_{21}–$2_{20}/3_{03}$–2_{02}, 4_{22}–$3_{21}/4_{04}$–3_{03}, and 4_{04}–$3_{03}/3_{03}$–2_{02} ratios. The gas kinetic temperatures derived from the para-H_2CO 3_{21}–$2_{20}/3_{03}$–2_{02} and 4_{22}–$3_{21}/4_{04}$–3_{03} line ratios are high, ranging from 43 to >300 K with an unweighted average of 91 ± 4 K. Deduced T_{kin} values from the $J=3$–2 and 4–3 transitions are similar. Spatial densities of the gas derived from the para-H_2CO 4_{04}–$3_{03}/3_{03}$–2_{02} line ratios yield 0.6–8.3×10^6 cm^{-3} with an unweighted average of $1.5\,(\pm0.1)\times10^6$ cm^{-3}. A comparison of kinetic temperatures derived from para-H_2CO, NH_3, and the dust emission indicates that para-H_2CO traces a distinctly higher temperature than the NH_3 (2,2)/(1,1) transitions and the dust, tracing heated gas more directly associated with the star formation process. The H_2CO linewidths are found to be correlated with bolometric luminosity and increase with the evolutionary stage of the clumps, which suggests that higher luminosities tend to be associated with a more turbulent molecular medium. It seems that the spatial densities measured with H_2CO do not vary significantly with the evolutionary stage of the clumps. However, averaged gas kinetic temperatures derived from H_2CO increase with time through the evolution of the clumps. The high temperature of the gas traced by H_2CO may be mainly caused by radiation from embedded young massive stars and the interaction of outflows with the ambient medium. For $L_{bol}/M_{clump}\gtrsim10\,L_\odot/M_\odot$, we find a rough correlation between gas kinetic temperature and this ratio, which is indicative of the evolutionary stage of the individual clumps. The strong relationship between H_2CO line luminosities and clump masses is apparently linear during the late evolutionary stages of the clumps, indicating that L_{H_2CO} does reliably trace the mass of warm dense molecular gas. In our massive clumps H_2CO line luminosities are approximately linearly correlated with bolometric luminosities over about four orders of magnitude in L_{bol}, which suggests that the mass of dense molecular gas traced by the H_2CO line luminosity is well correlated with star formation.

# Emission from magnetized accretion disks around young stars

C. Tapia1 and S. Lizano1

We calculate the emission of protoplanetary disks threaded by a poloidal magnetic field and irradiated by the central star. The radial structure of these disks was studied by Shu and collaborators and the vertical structure was studied by Lizano and collaborators. We consider disks around low mass protostars, T Tauri stars, and FU Ori stars with different mass-to-flux ratios λ_{sys}. We calculate the spectral energy distribution and the antenna temperature profiles at 1 mm and 7 mm convolved with the ALMA and VLA beams. We find that disks with weaker magnetization (high values of λ_{sys}) emit more than disks with stronger magnetization (low values of λ_{sys}). This happens because the former are denser, hotter and have larger aspect ratios, receiving more irradiation from the central star. The level of magnetization also affects the optical depth at millimeter wavelengths, being larger for disks with high λ_{sys}. In general, disks around low mass protostars and T Tauri stars are optically thin at 7 mm while disks around FU Ori are optically thick. A qualitative comparison of the emission of these magnetized disks, including heating by an external envelope, with the observed millimeter antenna temperature profiles of HL Tau indicates that large cm grains are required to increase the optical depth and reproduce the observed 7 mm emission at large radii.
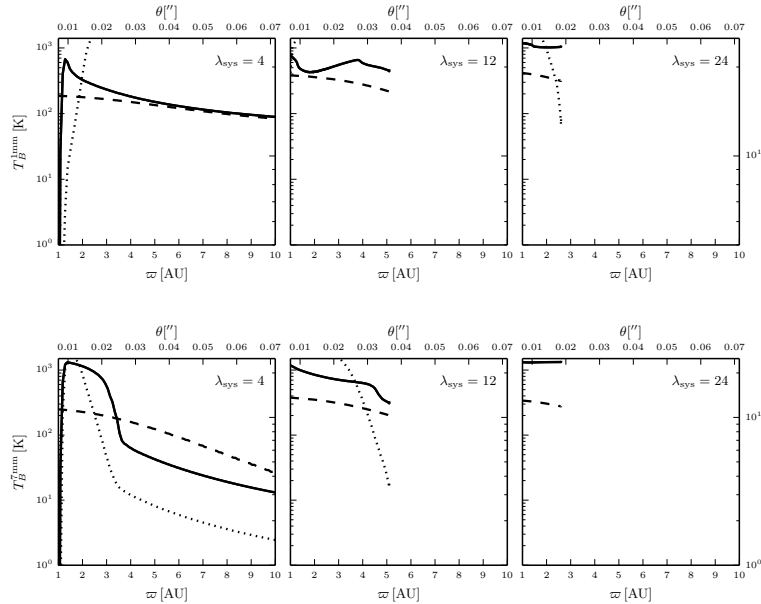
Table 1. YSOs parameters

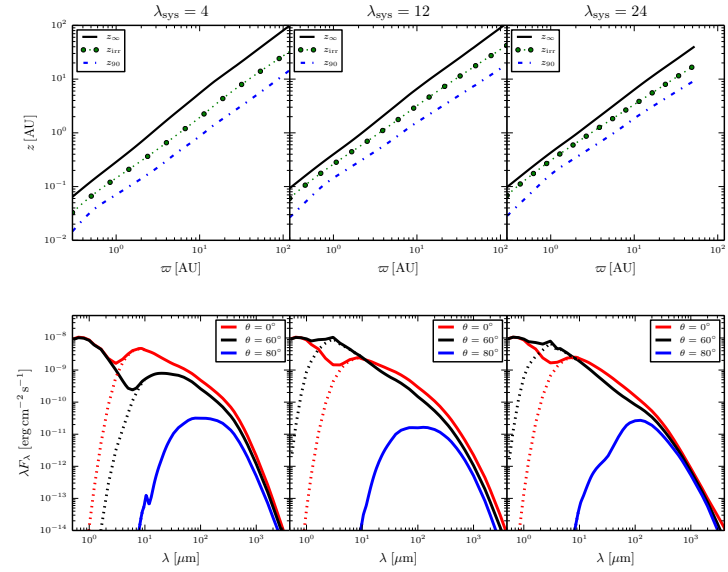| YSO	$\dot{M}_d$ $(M_\odot\mathrm{yr}^{-1})$	M_d $(M_\odot)$	R_* $(R_\odot)$	L_c $(L_\odot)$
LMP	2×10^{-6}	0.20	3	7.1
T Tauri	1×10^{-8}	0.03	2	0.93
FU Ori	2×10^{-4}	0.02	7	230
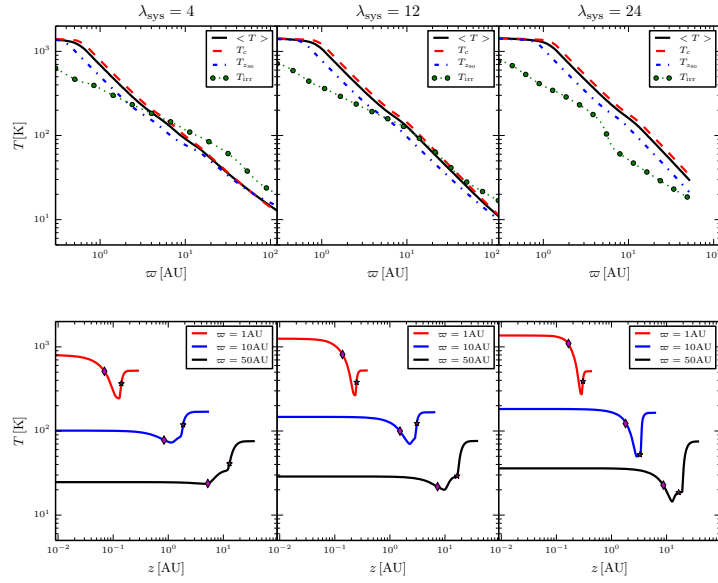
Figure 1. LMP disk models with different mass-to-flux ratios, $\lambda_{sys} = 4, 12, 24$, that label each column. The upper panels show the radial temperature profiles of the disks: the solid black lines correspond to the mass weighted temperature $< T >$; the red dashed lines show the mid-plane temperature T_c; the blue dot-dashed lines show the temperature of mass surface z_{90}; the green dot lines show the temperature at the irradiation surface z_{irr}. The lower panels show vertical temperature structure at the radii indicated in the upper right boxes. The star symbol corresponds to the location of the irradiation surface z_{irr} and the diamond symbol corresponds to the location of the mass surface z_{90}.
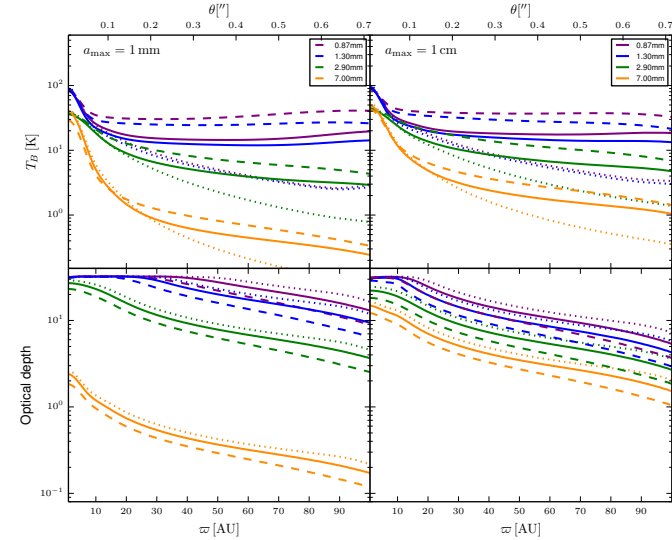
Figure 2. LMP disk models with different mass-to-flux ratios, $\lambda_{sys} = 4, 12, 24$, that label each column. The upper panels show the the different surfaces: the black solid lines show the surface of the disk z_{∞}; the green dot lines show the irradiation surface z_{irr}; the blue dot-dashed lines show the disk mass surface z_{90}. The lower panels show the spectral energy distribution (SED) of the star plus disk system at different inclination angles θ between the disk rotation axis and the l.o.s.: $\theta = 0°$, $60°$, and $80°$ (red, black and blue lines, respectively). The dotted lines show the disk contribution.

Figure 11. Antenna temperature T_B and optical depth τ_λ at 1 mm and 7 mm of FU Ori disks with different mass-to-flux ratios, $\lambda_{sys} = 4, 12, 24$, as a function of distance to the central star. The description of the panels and the lines is the same as in Figure 9. The upper middle panel and the lower right hand panel do not show the optical depth profile because, for numerical convenience, the integration of the optical depth ends at the value 25.

Figure 12. Antenna temperature T_B and optical depth τ_λ at 0.87, 1.3, 2.9, and 7 mm of LMP disks as a function of distance to the central star. The radial profiles have been convolved with the ALMA beams: $\theta_{0.87\,mm} = 0.034''$, $\theta_{1.3\,mm} = 0.029''$, $\theta_{2.9\,mm} = 0.066''$, and the VLA beam at 7 mm, $\theta_{7\,mm} = 0.043''$. The color code is shown in the boxes in the upper right corners. This color code is similar to the one used in Figure 3 of Carrasco-González et al. (2016) that plots the observed ALMA and VLA antenna temperature profiles of HL Tau. The disks have a mass-to-flux ratio $\lambda_{sys} = 24$. The disk parameters are shown in Table 4. The upper panels show T_B and the lower panels show τ_λ for each wavelength. The left panels correspond to models with a dust grain distribution with $a_{max} = 1$ mm: Model I (dotted lines) without envelope heating ($T_e = 0$ K); Model II (solid lines) with $T_e = 50$ K; Model III (dashed lines) with $T_e = 100$ K. The right panels correspond to models with $a_{max} = 1$ cm: Model IV (dotted lines) without envelope heating ($T_e = 0$ K); Model V (solid lines) with $T_e = 50$ K; Model VI (dashed lines) with $T_e = 100$ K.

300 Transient events in bright debris discs: Collisional avalanches revisited

#56 Philippe Thebault1 and Quentin Kral2
A&A

A collisional avalanche is set off by the breakup of a large planetesimal, releasing vast amounts of small unbound grains that enter a debris disc located further away from the star, triggering there a collisional chain reaction that could potentially create detectable transient structures. We investigate this mechanism, using for the first time a fully self-consistent code coupling dynamical and collisional evolutions. We also quantify for the first time the photometric evolution of the system and investigate if avalanches could explain the short-term luminosity variations recently observed in some extremely bright debris discs. We use the state-of-the-art LIDT-DD code (Kral et al., 2013, 2015). We consider an avalanche-favouring A6V star, and two set-ups: a "cold disc" case, with a dust release at 10 au and an outer disc extending from 50 to 120 au, and a "warm disc" case with the release at 1 au and a 5-12 au outer disc. We explore, in addition, two key parameters, which are the density (parameterized by its optical depth τ) of the main outer disc and the amount of dust released by the initial breakup. We find that avalanches could leave detectable structures on resolved images, for both "cold" and "warm" disc cases, in discs with τ of a few 10^{-3}, provided that large dust masses ($\gtrsim 10^{20}$–5×10^{22}g) are initially released. The integrated photometric excess due to an avalanche is relatively limited, less than 10% for these released dust masses, peaking in the $\lambda \sim 10$–20μm domain and becoming insignificant beyond ~ 40–50μm. Contrary to earlier studies, we do not obtain stronger avalanches when increasing τ to higher values. Likewise, we do not observe a significant luminosity deficit, as compared to the pre-avalanche level, after the passage of the avalanche. These two results concur to make avalanches an unlikely explanation for the sharp luminosity drops observed in some extremely bright debris discs. The ideal configuration for observing an avalanche would be a two-belt structure, with an inner belt (at ~ 1 or ~ 10au for the "warm" and "cold" disc cases, respectively) of fractional luminosity $f \geq 10^{-4}$ where breakups of massive planetesimals occur, and a more massive outer belt, with τ of a few 10^{-3}, into which the avalanche chain reaction develops and propagates.
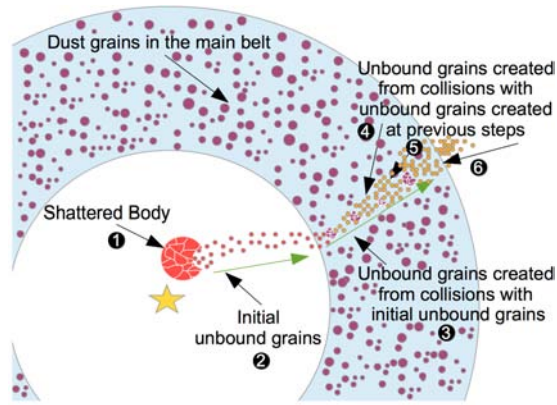
Fig. 1. Schematic description of the avalanche process. First, a large body is shattered in the inner region of the planetary system, releasing very small unbound grains that are blown out by radiation pressure. Then these small grains penetrate an outer disc located further away from the star. There they will collide, at very high velocities, with "native" target grains, producing a new generation of small unbound grains, which will also be blown out and collide with other target grains in the disc, creating new fragments, etc.. If the main disc is dense enough, this chain reaction can produce an excess of small grains largely exceeding the amount initially produced by the breakup.
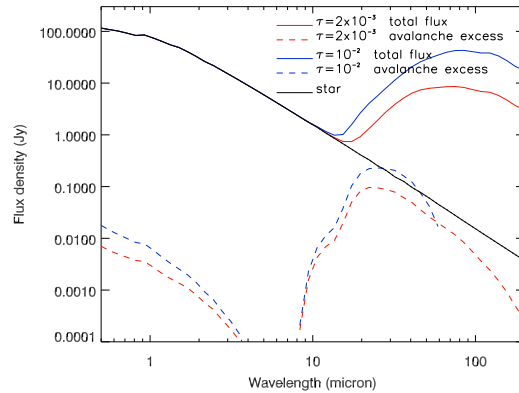
Fig. 8. Cold disc case: system-integrated SED (using the GRaTer package for a system at a distance of 30pc), at the peak of the avalanche luminosity, for the reference GAT07 $\tau_\perp \sim 2\times10^{-3}$ disc and for a denser $\tau_\perp \sim 10^{-2}$ disc. The dashed lines give the luminosity excess due to the avalanche (computed by subtracting the SED of a reference avalanche-free case). The cutoff of the dashed-blue line beyond 50μm reflects the fact that, for this dense disc case, the avalanche-system is slightly less luminous, at these long wavelengths, than an avalanche-free counterpart. This is because, beyond 50μm, the flux is mostly dominated by large grains, which are slightly eroded by the passage of the avalanche (see discussion in Sec.4.4.1)
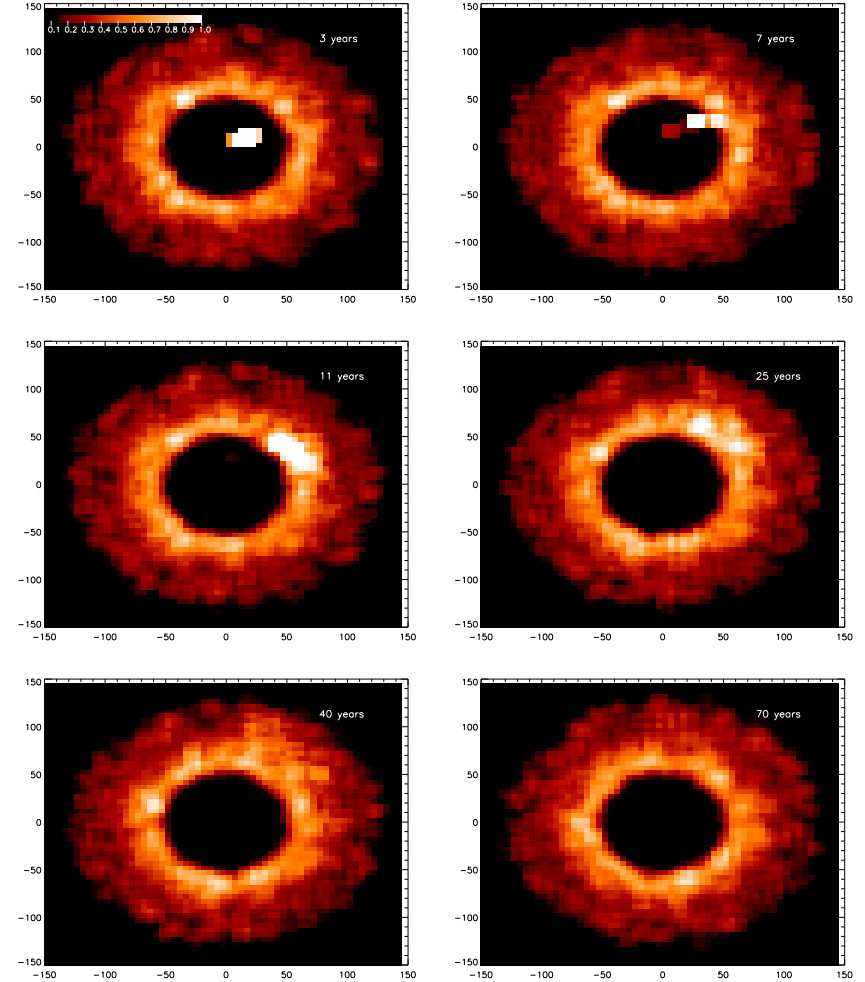

Fig. 3. Normalized synthetic images, in scattered light, showing the evolution of an avalanche in a cold debris disc (extending from 50 to 120 au) of average optical depth $\tau_\perp \sim 2\times10^{-3}$, for an initial breakup, at $t=0$, releasing 5×10^{22}g of dust at 10 au from the star.

## 300 Non-linear Development of Secular Gravitational Instability in Protoplanetary Disks

#57 Ryosuke T. Tominaga1, Shu-ichiro Inutsuka1, Sanemichi Z. Takahashi2,3,4
PASJ

We perform non-linear simulation of secular gravitational instability (GI) in protoplanetary disks that has been proposed as a mechanism of the planetesimal formation and the multiple ring formation. Since the timescale of the growth of the secular GI is much longer than the Keplerian rotation period, we develop a new numerical scheme for a long term calculation utilizing the concept of symplectic integrator. With our new scheme, we first investigate the non-linear development of the secular GI in a disk without a pressure gradient in the initial state. We find that the surface density of dust increases by more than a factor of one hundred while that of gas does not increase even by a factor of two, which results in the formation of dust-dominated rings. A line mass of the dust ring tends to be very close to the critical line mass of a self-gravitating isothermal filament. Our results indicate that the non-linear growth of the secular GI provides a powerful mechanism to concentrate the dust. We also find that the dust ring formed via the non-linear growth of the secular GI migrates inward with a low velocity, which is driven by the self-gravity of the ring. We give a semi-analytical expression for the inward migration speed of the dusty ring.
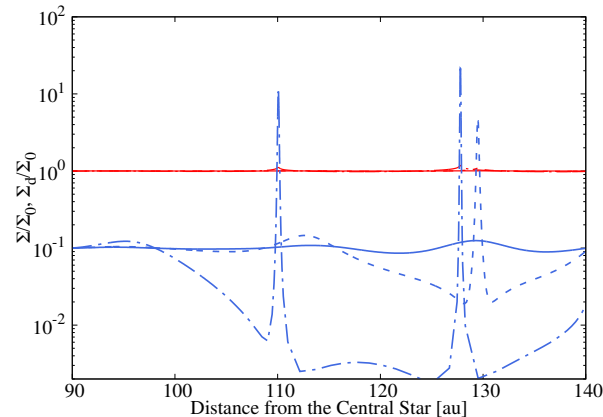
Fig. 8. Snapshot of the distribution of the surface densities of dust and gas. The thick blue line shows the surface density of dust, the thin red line shows that of gas. Both of them are normalized by the unperturbed surface density of gas. The solid, dashed and dotted-dashed lines show the surface density distribution at $t = 26148$ yr, 36479 yr, 54689 yr respectively. The most unstable mode of the secular GI at $r = 110$ and 130 au grows. While the gas surface density does not almost increase, the dust surface density becomes a hundred times larger than the initial surface density.
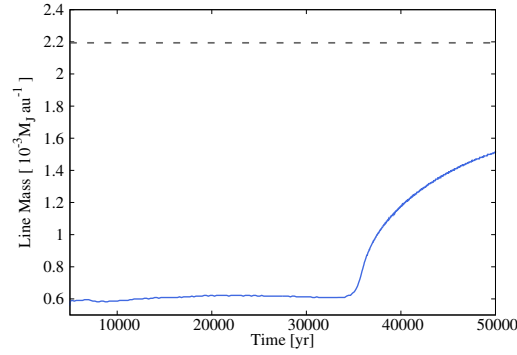
Fig. 10. Time evolution of the line mass of the dust ring. The solid line shows the line mass of the dust ring, and the dashed line shows the critical line mass of filament in which a sound velocity is equal to c_d we used in this work. We find that the line mass of the dust ring formed by the secular GI is comparable to the critical line mass.
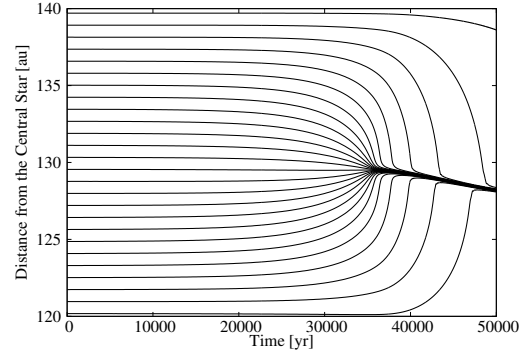
Fig. 11. Time evolution of positions of dust cells. We reduce the number of cells in the plot. Because we solve the evolution with the Lagrangian fluid equation, the more cells there are, the larger the surface density is. The radius where the cells concentrate represents the radius of the ring. We can see that the ring moves inward after it forms.
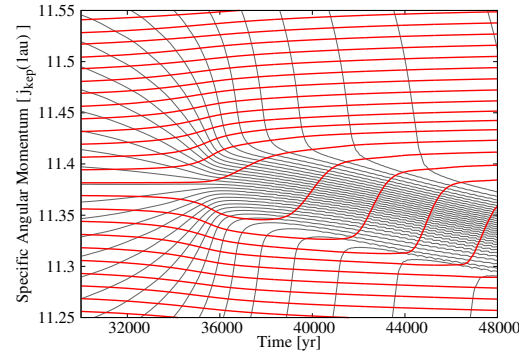
Fig. 12. Time evolution of specific angular momentums of dust and gas. The thin gray line represents that of dust, the thick red line represent that of gas. The vertical axis shows the specific angular momentum normalized by the Keplerian specific angular momentum $j_{kep}(r)$ at $r = 1$au. We reduce the number of cells we plot here with a constant interval. The specific angular momentum of dust decreases with the dust ring migrating, while that of gas increases when the dust ring passes through. The high dust-to-gas ratio in the ring results in larger rate of change of specific angular momentum of gas than that of dust.

300 Implications for planetary system formation from interstellar object 1I/2017 U1
#58 ('Oumua- mua)

David E. Trilling1, Tyler Robinson1, Alissa Roegge1, Colin Orion Chandler1, Nathan Smith1, Mark Loeffler1, Chad Trujillo1, Samuel Navarro-Meza1,2 and Lori M. Glaspie1

The recently discovered minor body 1I/2017 U1 ('Oumuamua) is the first known object in our Solar System that is not bound by the Sun's gravity. Its hyperbolic orbit (eccentricity greater than unity) strongly suggests that it originated outside our Solar System; its red color is consistent with substantial space weathering experienced over a long interstellar journey. We carry out an simple calculation of the probability of detecting such an object. We find that the observed detection rate of 1I-like objects can be satisfied if the average mass of ejected material from nearby stars during the process of planetary formation is ~20 Earth masses, similar to the expected value for our Solar System. The current detection rate of such interstellar interlopers is estimated to be 0.2/year, and the expected number of detections over the past few years is almost exactly one. When the Large Synoptic Survey Telescope begins its wide, fast, deep all-sky survey the detection rate will increase to 1/year. Those expected detections will provide further constraints on nearby planetary system formation through a better estimate of the number and properties of interstellar objects.

300 The VLA Nascent Disk And Multiplicity Survey of Perseus Protostars (VANDAM). III.
#59 Extended Radio Emission from Protostars in Perseus

Lukasz Tychoniec1,2, John J. Tobin1,3, Agata Karska4, Claire Chandler5, Michael M. Dunham6,7, Zhi- Yun Li8, Leslie W. Looney9, Dominique Segura-Cox9, Robert J. Harris9, Carl Melis10 and Sarah I. Sadavoy11

Centimeter continuum emission from protostars offers insight into the innermost part of the outflows, as shock-ionized gas produces free-free emission. We observed a complete population of Class 0 and I protostars in the Perseus molecular cloud at 4.1 cm and 6.4 cm with resolution and sensitivity superior to previous surveys. From a total of 71 detections, 8 sources exhibit resolved emission at 4.1 cm and/or 6.4 cm. In this paper we focus on this sub-sample, analyzing their spectral indices along the jet, and their alignment with respect to the large-scale molecular outflow. Spectral indices for fluxes integrated toward the position of the protostar are consistent with free-free thermal emission. The value of the spectral index along a radio jet decreases with distance from the protostar. For six sources, emission is well aligned with the outflow central axis, showing that we observe the ionized base of the jet. This is not the case for two sources, where we note misalignment of the emission with respect to the large-scale outflow. This might indicate that the emission does not originate in the radio jet, but rather in an ionized outflow cavity wall or disk surface. For five of the sources, the spectral indices along the jet decrease well below the thermal free-free limit of -0.1 with $> 2\sigma$ significance. This is indicative of synchrotron emission, meaning that high energy electrons are being produced in the outflows close to the disk. This result can have far-reaching implications for the chemical composition of the embedded disks.

Table 1. Properties of powering sources of resolved jets

Source	Region	Other names[a]	Class[b]	L_{bol}[b] $L_\odot$	T_{bol}[b] K	PA[c] °
Per-emb-8	IC 348	PER22, IC 348a, IRAS 03415+3152, YSO 48	0	2.6±0.5	43.0±6.0	135 (5)
Per-emb-18	NGC 1333	NGC 1333 IRAS7, YSO 24	0	2.8±1.7	59.0±12.0	159 (2)
Per-emb-20	L1455	L1455-IRS4	0	1.4±0.2	65.0±3.0	115 (2)
Per-emb-30	B1	PER19, B1 SMM11, YSO 40	0/I	1.1±0.0	93.0±6.0	109 (2)
Per-emb-33	L1448	PER02, L1448 N(A), L1448 IRS3B, YSO 2	0	8.3±0.8	57.0±3.0	105 (3)
Per-emb-36	NGC 1333	PER06, NGC 1333 IRAS2B, YSO 16	I	6.9±1.0	85.0±12.0	24 (1)
L1448 IRS3A	L1448	-	I	9.2±1.3	47.0±2.0	38 (4)
SVS 13C	NGC 1333	VLA2	0	1.5±0.2	21.0±1.0	8 (1)

[a] Names: YSOXX - Jørgensen et al. (2007), PERXX - Karska et al. (2014), VLAXX - Rodríguez et al. (1997)

[b] References: Enoch et al. (2009), Sadavoy et al. (2014)

[c] References: (1) Plunkett et al. (2013), (2) Davis et al. (2008), (3) Kwon et al. (2006), (4) Lee et al. (2016), (5) Tobin et al. in prep.
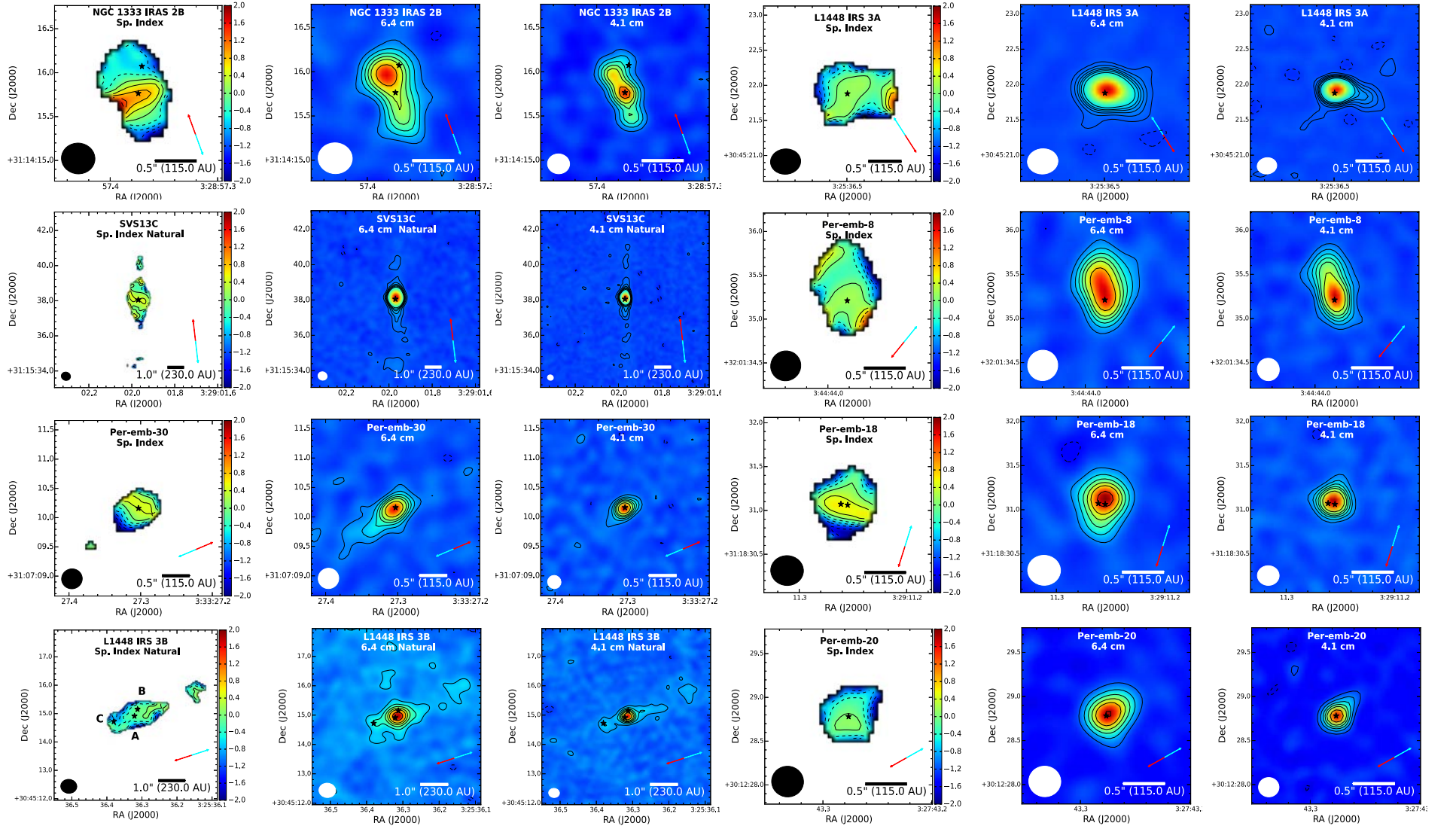
Figure 1. Images of Per-emb-36. Spectral index map with contours [-2.0, -1.6, -1.2, -0.8, -0.4, 0.0, 0.4, 0.8, 1.2, 1.6, 2.0]. 6.4 cm and 4.1 cm maps with contours [-3, 3, 6, 9, 12, 15, 20] x σ where $\sigma_{6.4\ cm} = 4.83\ \mu$Jy and $\sigma_{4.1\ cm} = 3.90\ \mu$Jy. Synthesized beam is shown in the left bottom corner (Sp. Index and 6.4 cm: $0\rlap{.}''41 \times 0\rlap{.}''35$, 4.1 cm: $0\rlap{.}''26 \times 0\rlap{.}''22$). The stars mark the position of the protostars based on Ka-band observations (Tobin et al. 2016b) and the red and blue arrows indicate outflow direction from Plunkett et al. (2013) with a position angle 24°. 6.4 cm and 4.1 cm maps are not corrected for a primary beam response (spectral index derived from PB corrected map).

300

#60

# High spectral resolution observations of HNC_3 and HCCNC in the L1544 prestellar core

C. Vastel1, K. Kawaguchi2, D. Quénard3, M. Ohishi4, B. Lefloch5, R. Bachiller6, H.S.P. Müller7

HCCNC and HNC_3 are less commonly found isomers of cyanoacetylene, HC_3N, a molecule that is widely found in diverse astronomical sources. We want to know if HNC_3 is present in sources other than the dark cloud TMC-1 and how its abundance is relative to that of related molecules. We used the ASAI unbiased spectral survey at IRAM 30m towards the prototypical prestellar core L1544 to search for HNC_3 and HCCNC which are by-product of the HC_3NH^+ recombination, previously detected in this source. We performed a combined analysis of published HNC_3 microwave rest frequencies with thus far unpublished millimeter data because of issues with available rest frequency predictions. We determined new spectroscopic parameters for HNC_3, produced new predictions and detected it towards L1544. We used a gas-grain chemical modelling to predict the abundances of N-species and compare with the observations. The modelled abundances are consistent with the observations, considering a late stage of the evolution of the prestellar core. However the calculated abundance of HNC_3 was found 5–10 times higher than the observed one. The HC_3N, HNC_3 and HCCNC versus HC_3NH^+ ratios are compared in the TMC-1 dark cloud and the L1544 prestellar core.

- IRAM 30m, Astrochemical Studies At IRAM (ASAI) unbiased spectral survey
- 実験室でのマイクロ波分光とミリ波天体観測の合わせ技で分子定数を決めてラインを同定し、prestellar core L1544でHNC₃を初めて検出
- Nを含む分子について、gas-grain chemical modellingと観測を比較
    - HC_3NH^+, HC_3N, HNC_3, HCCNCはコアの外縁部（他の分子でnon-thermal desorptionが見られる）から出ている
    - L1544がprestellar core後期の段階にあることを考慮すると、モデルの予想は観測された強度とコンシステント（例外：HNC_3）
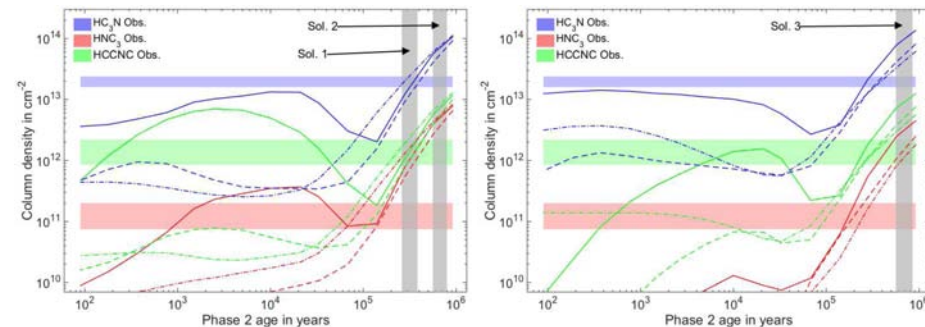
Figure 3. Column densities for HC_3N, HNC_3 and HCCNC as a function of the age of the phase 2 for different initial gas densities of the ambient cloud phase: 10^2 cm^{-3} (full line), 3×10^3 cm^{-3} (dashed line), and 2×10^4 cm^{-3} (dash-dotted line). The area of confidence of the observed column densities for these species is also shown. Grey areas shows the timespan area of confidence of each model based on the observed $HCNH^+$. These areas are labelled solutions 1, 2 and 3 (Quénard et al. 2017). *Left panel:* Model EA1 of initial atomic abundances ("low-metal abundances"). *Right panel:* Model EA2 of initial atomic abundances ("high-metal abundances"). All the informations on the modelling can be found in Quénard et al. (2017).